Journal of Zhejiang University-SCIENCE A (Applied Physics & Engineering) 2023 24(4):350-365
www.jzus.zju.edu.cn; www.springer.com/journal/11582
E-mail: jzus_a@zju.edu.cn

Research Article

https://doi.org/10.1631/jzus.A2200286

Discrete element method study of hysteretic behavior and deformation characteristics of rockfill material under cyclic loading

Mingchun LIN[1,2], Guanqi WANG[3], Jian ZHOU[4], Wei ZHOU[1,2]✉, Ni AN[1,2], Gang MA[1,2]

[1]*State Key Laboratory of Water Resources and Hydropower Engineering Science, Wuhan University, Wuhan 430072, China*
[2]*Institute of Water Engineering Sciences, Wuhan University, Wuhan 430072, China*
[3]*Power China Chengdu Engineering Co., Ltd., Chengdu 610072, China*
[4]*Power China Kunming Engineering Co., Ltd., Kunming 650051, China*

Abstract: Granular geomaterials under different loading conditions manifest various behaviors, such as hysteresis. Understanding their hysteretic behavior and deformation characteristics is the basis for establishing a constitutive relation with excellent performance in deformation prediction. The deformation characteristics of crushable particle materials are analyzed through a series of cyclic loading tests conducted by numerical simulation. The hysteretic behavior is investigated from a particle scale. The increase in particles with contacts less than two may be responsible for the residual strain, and the particle breakage further promotes particle rearrangement and volume contraction. Both the accumulation of plastic strain and the resilient modulus are found to be related to confining pressures, stress levels, cyclic loading amplitudes, and the number of cycles. The plastic strain accumulation can be written as a function of the number of cycles and an evolution function of resilient modulus is proposed.

Key words: Granular material; Discrete element method (DEM); Plastic deformation; Cyclic loading; Hysteretic behavior

1 Introduction

Granular geomaterials, such as rockfills, sands, and soils, are discrete in nature and widely used in geotechnical engineering. Their mechanical behaviors are highly nonlinear when subjected to complex loading conditions. Cyclic loading and its impacts are of practical relevance for many problems in geotechnical engineering. For example, the periodic change in reservoir water levels causes dams to suffer from cyclic loading. For the earth-rockfill dam, the fluctuation of water level often causes large deformation of the dam body and dam slope instability (Zhou et al., 2016a, 2016b; Zhang et al., 2022). For the concrete face slab rockfill dam, the frequent change in reservoir water levels also has an impact on the deformation of the dam body and the concrete face slab (Scaioni et al., 2018).

✉ Wei ZHOU, zw_mxx@whu.edu.cn
Mingchun LIN, https://orcid.org/0000-0002-2587-0155
Wei ZHOU, https://orcid.org/0000-0003-3607-1794

Received May 31, 2022; Revision accepted Sept. 8, 2022;
Crosschecked Feb. 24, 2023

A remarkable feature of granular geomaterials is that the stress–strain curve forms a so-called hysteresis loop during the cyclic loading (Fig. 1). The hysteresis loops will get close to and overlap each other after a sufficient number of cycles. The hysteretic behavior and accompanied strain accumulation caused by cyclic loading are the primary concerns for the deformation and settlement of geotechnical structures (Lobo-Guerrero and Vallejo, 2006; Liu H et al., 2018). Generally, the deformation estimation of geomaterials such as rockfill material is on the basis of compressibility tests (Skrzypkowski, 2020, 2021). Previous experimental studies have found that the hysteretic behaviors of granular geomaterials depend on many factors, such as confining pressure, cyclic vertical stress ratio, the number of cycles, the amplitude of a cycle, principal stress rotation, and aggregate degradation (Indraratna et al., 2010; Sun et al., 2014; Cai et al., 2015; Gu et al., 2020). The hysteretic behavior manifests nonlinear deformation and the irreversible evolution of plastic strain. The large-scale cyclic triaxial tests indicate that the strain of rockfill material under cyclic loading can be decomposed into a cyclic part and a residual part, where the residual plastic strain

increases rapidly only during the first few cycles (Fu et al., 2017; Zhang LK et al., 2019). Besides, particle breakage only occurs during the first cycle, and the permanent deformation during cyclic loading can be attributed to the initial breakage and subsequent rearrangement of the broken particles (Dahal and Mishra, 2020). However, the cyclic triaxial tests of rockfills are subject to difficult sample preparation, and more information and underlying mechanisms are not easily discovered.

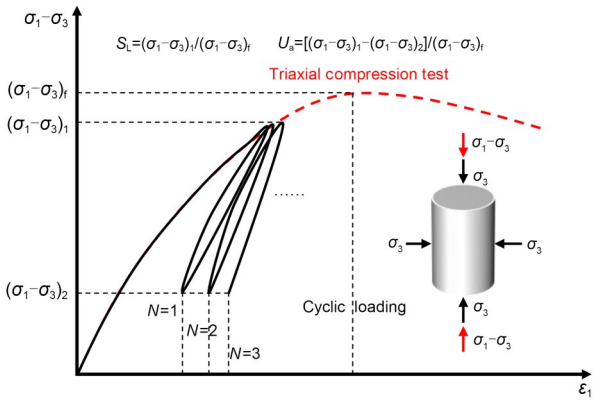

Fig. 1 Typical stress–strain responses of granular media: cyclic loading (solid line) and conventional triaxial compression test (dashed line). S_L and U_a represent the stress level and the amplitude of cyclic loading, respectively; N is the number of cycles; ε_1 is the axial strain; σ_i (i=1, 2, 3) corresponds to the principal values of the particle stress tensor; the subscript of $(\sigma_1-\sigma_3)$ corresponds to the deviatoric stress when N=1, 2, ⋯; $(\sigma_1-\sigma_3)_f$ corresponds to the peak stress state in triaxial compression test

Limited by apparatus size, measurement accuracy, and experimental cost, the cyclic triaxial test of rockfills with many cycles is hard to conduct in the laboratory. However, with the aid of numerical simulation techniques, the mechanism responsible for the hysteretic behavior of granular materials has been investigated (Sazzad and Suzuki, 2011; Sazzad, 2014; Xia et al., 2021; Lin et al., 2022), and even large deformation geotechnical problems can be further analyzed (Jin et al., 2021; Yin et al., 2021; Yuan et al., 2021). The contact structure and particle arrangement are found to be closely related to the hysteretic behavior of granular materials. For example, the contact fabric of granular materials shows different degrees of anisotropy during loading and unloading (Sazzad, 2014), which implies residual deformation at the microscale. Also, the particle interlocking effect induced by interparticle friction and particle shape significantly influences the hysteretic behavior and energy dissipation of granular materials (Lu and McDowell, 2007; O'Sullivan et al., 2008; Athanassiadis et al., 2014). It was found that the width of the hysteresis loop is related to interparticle friction and the internal inherent anisotropy caused by the particle bedding direction (Sazzad and Suzuki, 2010, 2011). On the other hand, granular materials are vulnerable to breakage and the stress strength and irreversible volumetric deformation will be influenced by the change in particle size distribution after particle crushing (Harireche and McDowell, 2003; Tapias et al., 2015; Zhou et al., 2016a, 2017; Ma et al., 2019). Moreover, particle breakage promotes particle rearrangement and further causes permanent deformation of granular materials under cyclic loading (Lobo-Guerrero and Vallejo, 2006; Zhang LK et al., 2019).

So far, most of the research concerning the properties of geomaterials under cyclic loading has focused on the dynamic responses and liquefication of sandy soils (Jiang et al., 2019; Wei et al., 2020). However, the deformation characteristics of rockfill material are different from those of sandy soils due to more significant particle breakage and state-dependent dilatancy (Xiao et al., 2016). Also, the deformation characteristics that geomaterials demonstrate when they suffer seismic or traffic vibrations (Liu et al., 2014; Chen et al., 2016) are different from cases under low-frequency cyclic loading (such as the change of water level in rockfill dam projects), and the latter are rarely discussed.

Many numerical methods can be used to investigate macroscopic and microscale mechanics of geomaterials with particle breakage considered. Discrete element method (DEM) and the combined finite-discrete element method (FDEM) are the two most widely used (Lobo-Guerrero and Vallejo, 2006; Ciantia et al., 2015; Ma et al., 2019; Chen et al., 2021). Although FDEM can obtain the crack propagation paths and the stress field inside an individual particle with complex shapes (Zhou et al., 2022), the great number of entity units and interface units involved in the simulation can bring significant computational costs. Compared to FDEM, DEM is able to capture the main mechanical characteristics of rockfill material with higher computational efficiency (Ciantia et al., 2015; Zhou et al., 2020).

This paper aims to study the deformation characteristics of rockfill material under cyclic loading and the hysteretic behavior from a macro and microscale perspective. To this goal, a series of 3D DEM numerical simulations including conventional triaxial compression tests and cyclic loading of rockfill material are conducted (Section 2). We investigate the deformation at the particle level and analyze the underlying mechanism of hysteretic behavior (Section 3). Then, the effects of different loading conditions on plastic strain accumulation and resilient modulus are discussed (Section 4). Finally, the main findings of this study are summarized (Section 5).

2 DEM simulation of cyclic triaxial test

2.1 Rolling resistance contact model

Particle rotations of geomaterials are usually limited during shearing, and the rolling resistance may be caused by surface roughness and shape irregularity (Estrada et al., 2011; Zhao et al., 2018). Many studies have found that macroscale mechanics and microstructures of geomaterials, such as stress strength, dilatancy, and fabric anisotropy, are quantitively influenced by rolling resistance (Belheine et al., 2009; Liu YM et al., 2018). Some mechanical behaviors observed in experiments are difficult to reproduce by the DEM simulation without the rolling resistance (Iwashita and Oda, 1998, 2000; Santos et al., 2020). Recently, the rolling resistance contact model has been widely used to imitate the rolling resistance of real particles in DEM simulation and its capability in reproducing the main features of granular materials has been proven (Estrada et al., 2011; Zhao et al., 2018; Zou et al., 2022). Since the effect of complex shapes on the macro mechanics of rockfill material is beyond the scope of this study, the rolling resistance linear model based on the papers of Ai et al. (2011) and Wensrich and Katterfeld (2012) is adopted to reflect the rolling resistance due to irregular shapes of rockfills.

The normal and tangential contact forces in the rolling resistance linear contact model follow the linear force–displacement law. The magnitude of normal contact force $\boldsymbol{F}_{\mathrm{n}}$ is proportional to the value of the contact overlap $\boldsymbol{U}_{\mathrm{n}}$, i.e., $\boldsymbol{F}_{\mathrm{n}}=k_{\mathrm{n}}\boldsymbol{U}_{\mathrm{n}}$. The normal stiffness k_{n} is computed as a function of the radii of two spherical particles, i.e.,

$$k_{\mathrm{n}}=\frac{\pi R^2 E^*}{R_1+R_2}, \tag{1}$$

where E^* is the effective modulus, R_1 and R_2 are the radii of two contacted particles, and R is the radius of the smaller particle. The tangential contact force $\boldsymbol{F}_{\mathrm{t}}$ is incremented as the relative shear–displacement during the timestep and it is also limited by Coulomb's friction $\boldsymbol{F}_{\mathrm{t}}\leqslant\mu\boldsymbol{F}_{\mathrm{n}}$ (μ is the particle friction coefficient). The normal-to-tangential stiffness ratio k^* is defined as $k^*=k_{\mathrm{n}}/k_{\mathrm{t}}$ (k_{t} is the tangential stiffness). Since DEM simulations in this study are performed by particle flow code in 3D (PFC3D), for more details about the rolling resistance contact model please refer to the PFC5.0 documentation (Itasca Consulting Group Inc., 2014).

To capture the rolling resistance of contact particles, the linear-accumulated relative rotation moment of particles at contact points is taken into account. The rolling resistance moment $\boldsymbol{M}_{\mathrm{r},t}$ is computed as:

$$\boldsymbol{M}_{\mathrm{r},t+\Delta t}=\begin{cases}\boldsymbol{M}_{\mathrm{r},t}-k_{\mathrm{r}}\Delta\boldsymbol{\theta}_{\mathrm{b}}, & \left\|\boldsymbol{M}_{\mathrm{r},t}-k_{\mathrm{r}}\Delta\boldsymbol{\theta}_{\mathrm{b}}\right\|\leqslant\mu_{\mathrm{r}}\bar{R}\boldsymbol{F}_{\mathrm{n}},\\ \mu_{\mathrm{r}}\bar{R}\boldsymbol{F}_{\mathrm{n}}\dfrac{\boldsymbol{M}_{\mathrm{r},t}-k_{\mathrm{r}}\Delta\boldsymbol{\theta}_{\mathrm{b}}}{\left\|\boldsymbol{M}_{\mathrm{r},t}-k_{\mathrm{r}}\Delta\boldsymbol{\theta}_{\mathrm{b}}\right\|}, & \text{otherwise,}\end{cases} \tag{2}$$

where k_{r}, μ_{r}, and $\Delta\boldsymbol{\theta}_{\mathrm{b}}$ are the rolling resistance stiffness, the rolling resistance coefficient, and the relative bend-rotation increment, respectively. The contact effective radius $\bar{R}$ is defined as $R_1R_2/(R_1+R_2)$.

2.2 Particle breakage strategy

There are two approaches to simulating the crushing process of granular materials in DEM simulation: the bonded-particle model (BPM) (Harireche and McDowell, 2003; Potyondy and Cundall, 2004) and the fragment replacement model (FRM) (Xu et al., 2020; Zhou et al., 2020). The BPM is to form large agglomerates by bonding many elementary spheres at contacts. It has advantages in considering particle shapes and simulating crack propagation (Huang et al., 2020). However, the large number of bonded particles will increase the computational cost when simulating a large-size specimen. The FRM is to replace the broken particle with a few small particles, which helps computational efficiency. Besides, fragment particles can break further which is not allowed in BPM. Therefore, the FRM is more suitable for the simulation of a

large number of crushable particles (Xu et al., 2020; Zhou et al., 2020) and it is adopted in this study.

Two issues need to be determined when the FRM is adopted, i.e., the particle breakage criterion and the fragment replacement mode. To determine whether particle breakage should occur or not, the octahedral shear stress criterion is adopted (Ben-Nun and Einav, 2010; de Bono and McDowell, 2016):

$$q=\frac{1}{3}\sqrt{(\sigma_1-\sigma_2)^2+(\sigma_2-\sigma_3)^2+(\sigma_3-\sigma_1)^2}, \quad (3)$$

where q is the octahedral shear stress. The average stress tensor of a particle with volume V_p is calculated as (Bagi, 1996):

$$\boldsymbol{\sigma}_{ij}=\frac{1}{V_p}\sum_{n_c}\boldsymbol{f}_i^c\boldsymbol{l}_j^c, \quad (4)$$

where n_c is the number of contacts of the particle; $\boldsymbol{f}_i^c$ is the contact force of the cth contact; $\boldsymbol{l}_j^c$ is the vector related to the centroids of two particles forming the cth contact.

When the octahedral shear stress q acting on a particle exceeds the predefined particle crushing strength $[q]$, the particle should break and be replaced by a group of smaller particles. The particle crushing strength is determined as (Lee, 1992; McDowell and Bolton, 1998):

$$[q]=\sigma_f=\frac{F_f}{r^2}, \quad (5)$$

where F_f is the peak load of the single-particle crushing compression test; r is the particle radius. The strength of rockfill particles yields the Weibull distributions (Zhou et al., 2019; Xiao et al., 2020), and the particle crushing strength σ_f can be calculated as:

$$\sigma_f=\left[\ln\left(\frac{1}{P_s(d)}\right)\right]^{\frac{1}{m}}\left(\frac{d}{d_0}\right)^{-\frac{n_d}{m}}\sigma_0, \quad (6)$$

where $P_s(d)$ is the particle survival probability with diameter d; m is the Weibull modulus, the value of n_d/m characterizes the size effect of particle crushing strength; σ_0 is the characteristic strength ($P_s(d)$= 37% for a sample of size d_0). The decrease in the minimum particle size in the system due to the fragment replacement will reduce the critical timestep (t_{crti}–(m_p/k)$^{0.5}$, where m_p is the mass of the smallest particle, and k is its stiffness) and raise the time consumption of simulation. To avoid an unlimited decrease in particle sizes and a high computational cost, the smallest breakable particle size is set to 8 mm in this study.

Choosing an appropriate fragment replacement mode is also important in the DEM simulation of particle breakage. One of the most used packing configurations for the fragment replacement is the apollonian sphere packing proposed by Ciantia et al. (2015). It has been verified that such sphere packing mode is sufficient to reproduce the mechanical behaviors of rockfill material due to its fractal dimension being close to the ultimate particle size distribution of the breakage-occurred granular assembly (Borkovec et al., 1994; Einav, 2007; Zhou et al., 2020). Various kinds of apollonian sphere packings with different numbers and sizes of particles can intuitively affect computational efficiency. Ciantia et al. (2015) reported that the arrangement of 14 non-overlapping tangent balls within a spherical space is enough for DEM simulation to reproduce the breakage behaviors of granular materials. Therefore, the fragment replacement mode of 14-ball with four sizes is employed when particle breakage occurs, and a graphical representation is shown in Fig. 2. Then, the apollonian sphere packing will be slowly expanded to meet the mass conservation. To avoid generating explosive local stress, the expansion process is gradually completed in four steps in this study. After the expansion, fragment particles are further allowed to relax large overlaps and release the extra kinetic energy. After the particle expansion is finished, the angular and translational velocity of particles whose velocities are too large will be set to zero to eliminate the kinetic energy of particles. The radii of the four-sized child particles are r_1=0.4641r_0, r_2= 0.3659r_0, r_3=0.2573r_0, and r_4=0.2240r_0, where r_0 is the radius of the parent particle.

2.3 Calibration of DEM parameters

The simulation parameters of rockfill material in this study are calibrated based on experimental data. A set of large-scale triaxial tests on limestones was performed on specimens of 300-mm diameter and 600-mm height. The specimen preparation and the drained-consolidation compression procedures were performed in accordance with the specification of soil

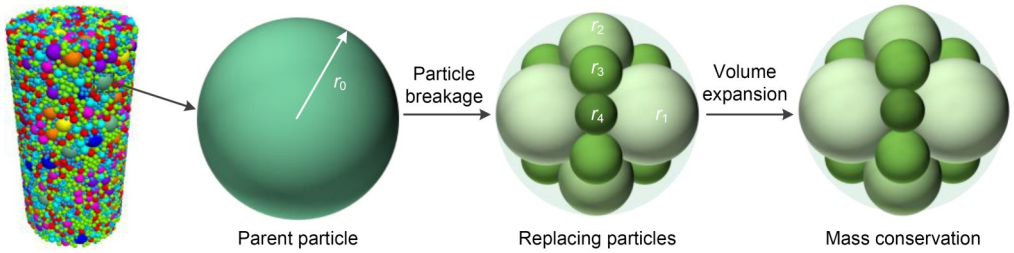

Fig. 2 Illustration of particle breakage modeling using fragment replacement method

test (MWR, 1999). The laboratory tests stopped when specimen failure or axial strains ε_1 reached 15%. To calibrate DEM parameters, the numerical tests are conducted on the same size as the experimental specimen. The laboratory triaxial apparatus and the numerical specimen are shown in Fig. 3.

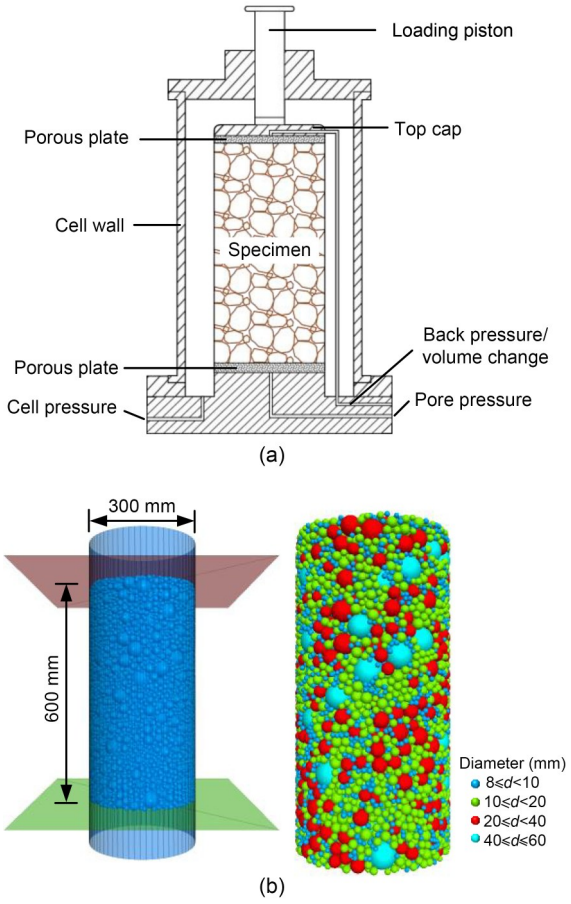

Fig. 3 Triaxial compression tests: (a) laboratory triaxial apparatus; (b) numerical specimen. References to color refer to the online version of this figure

The particle sizes follow the fractal size distribution for the range d_{min}–d_{max} (Einav, 2007):

$$\frac{M_d(x<d)}{M_T}=\frac{d^{3-D}-d_{min}^{3-D}}{d_{max}^{3-D}-d_{min}^{3-D}}, \tag{7}$$

where $M_d(x<d)$ is the cumulative mass percentage of particles with sizes less than d, and M_T is the total mass of the particle assembly. In this study, the fractal dimension D=2.6, the minimum particle size d_{min}= 8 mm, and the maximum particle size d_{max}=60 mm. The particle size distribution and frequency curves (F_{accum} means the accumulative frequency by the number of particles N_p) are presented in Fig. 4.

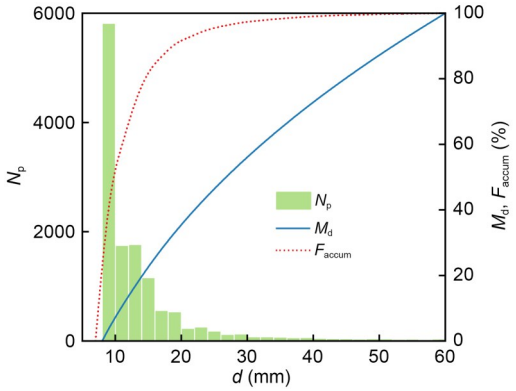

Fig. 4 Particle size distribution and frequency curves

The simulation specimen is enclosed by a cylindrical lateral wall and a pair of plates at the top and bottom, and a rigid boundary is adopted. To obtain an initial porosity of 0.3, particles are randomly generated in a cuboid with the same height and volume as the cylindrical specimen and contracted into the cylinder by scaling their locations. Then particles are allowed to relax to eliminate large overlaps. After removing particles outside the cylinder, there are 12596 particles in the specimen. The rolling resistance coefficient is set to zero during the specimen preparation. The stiffness of the cylindrical wall is set to 5% of the stiffness of particles to simulate the flexible membrane.

The specimen is consolidated to the target confining pressure by servo control. Applying the confining pressure consists of two steps: (i) pre-compressing the specimen to $\sigma_2=\sigma_3=(100.0\pm0.5)$ kPa with specimen stabilization achieved; (ii) applying the confining pressure and maintaining it at the preset value (tolerance of 0.5%). When the consolidation is completed, the upper and lower plates are vertically moved to compress the specimen. The servo control still works to keep the confining pressure constant during the compression process. The inertial number $I=\dot{\varepsilon}\bar{d}\sqrt{\rho/p}$ is much less than 10^{-3} to ensure the quasi-static loading, where $\dot{\varepsilon}$ is the strain rate, $\bar{d}$ is the average particle diameter, ρ is the particle density, and p is the mean stress.

The parameters in the linear resistance contact model that need to be calibrated include the effective modulus E^*, normal-to-tangential stiffness ratio k^*, rolling resistance coefficient μ_r, and friction coefficient μ. Using a trial-and-error approach, triaxial simulations of rockfill material under different confining pressures are conducted to calibrate the input parameters. As shown in Fig. 5, the simulated stress–strain curves coincide well with the experimental results, which verifies the reliability of the chosen parameters. The calibrated parameters are summarized in Table 1.

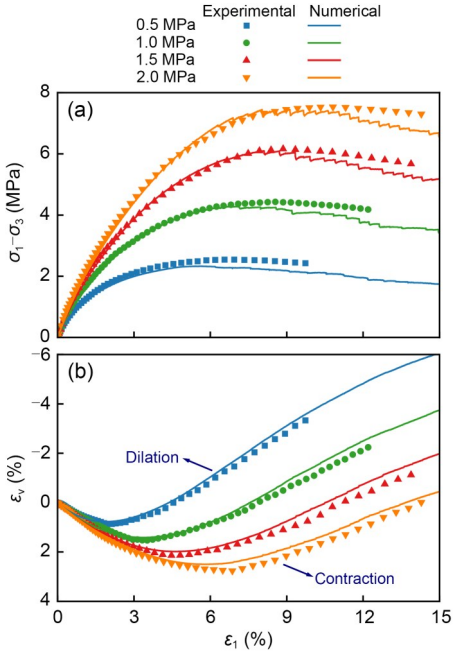

Fig. 5 Calibration of DEM parameters: (a) deviatoric stress evolution; (b) volumetric strain (ε_v) evolution. References to color refer to the online version of this figure

Table 1 Input parameters of DEM simulation

Parameter	Value
Density, ρ (kg/m^3)	2220
Effective modulus, E^* (MPa)	3.85
Characteristic particle size, d_0 (mm)	28.0
Normal stiffness, k_n (MPa)	1.0
Normal-to-tangential stiffness ratio, k^*	1.0
Sliding friction coefficient, μ	0.352
Rolling resistance coefficient, μ_r	0.90
Characteristic strength (MPa), σ_0	12.0
Weibull modulus, m	2.65
Plate velocity, v (m/s)	0.05

2.4 Cyclic loading

We systematically investigate the effects of confining pressure P, stress level S_L, the amplitude of cyclic loading U_a, and the number of cycles N on the mechanical behaviors of rockfill material. A series of cyclic loading simulations with different loading combinations are carried out. The sample preparation process is the same as that of the conventional triaxial test. The settings of loading conditions are summarized in Table 2. For each cyclic loading test, the specimen is first isotropically compressed to the expected confining pressure by servo control. Then, the specimen is compressed to the corresponding stress level and unloaded at the prescribed amplitude of cyclic loading before the next round of loading. All cyclic loading tests follow the same simulation process until the number of cycles reaches 50.

Table 2 Loading conditions of cyclic loading simulations

Loading condition	Value
Confining pressure, P (MPa)	0.5, 1.0, 1.5, 2.0
Stress level, S_L	0.25, 0.5, 0.7, 0.9
Amplitude of cyclic loading, U_a	0.25, 0.5, 0.75, 1.0
Number of cycles, N	50

For brevity, the stress and strain responses of only two cyclic loading tests are presented in Fig. 6, and the rest have a similar evolution which will be discussed in a later section. As seen in Figs. 6a and 6c, hysteresis loops are formed due to the nonlinearity of rockfill particles. Also, the formation of hysteresis loops suggests the generation of new plastic deformations. It is significant that the hysteresis loops are almost parallel to each other which means the resilient moduli have little change during the cyclic loading

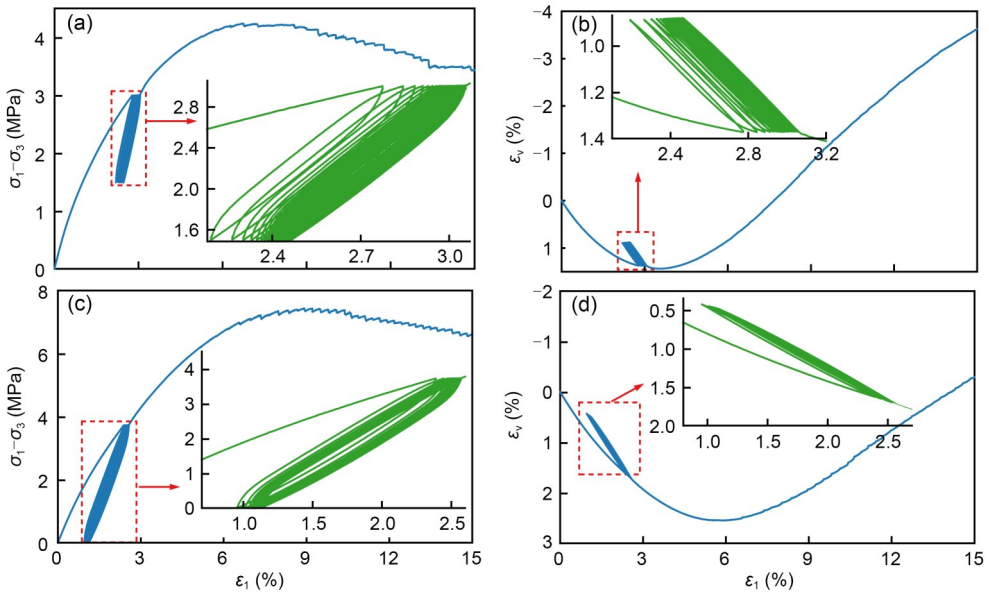

Fig. 6 Evolution of shear stresses (a and c) and volumetric strains (b and d) for crushable granular materials under different cyclic loading conditions: (a and b) P=1.0 MPa, S_L=0.7, and U_a=0.5; (c and d) P=2.0 MPa, S_L=0.5, and U_a=1.0

process. The hysteresis loops gradually overlap as the number of cycles increases, suggesting that there are no new plastic deformations produced after a certain number of cyclic loadings. Besides, the shapes and the areas of the loops in the two simulations are different which shows that the hysteretic behavior is closely linked to confining pressures, stress levels, and the amplitudes of cyclic loadings.

The volumetric strain curves also have obvious hysteretic behavior. Both specimens show dilatancy after cyclic loading, but the specimen under higher confining pressure (P=2.0 MPa) shows more apparent volumetric shrinkage as well as hysteretic behavior.

3 Hysteretic behavior from a microscale perspective

Generally, the axial strain can be decomposed into elastic strain and accumulated plastic strain, i.e., $\varepsilon_1=\varepsilon_1^e+\varepsilon_1^p$; similarly, volumetric strain can be written as $\varepsilon_v=\varepsilon_v^e+\varepsilon_v^p$. In a cycle of loading and unloading (Fig. 7a), the incremental axial strain is $\Delta\varepsilon_1=\varepsilon_C-\varepsilon_A$, the recoverable strain is $\Delta\varepsilon_1^e=\varepsilon_C-\varepsilon_D$, and the incremental plastic strain $\Delta\varepsilon_1^p$ equals $\varepsilon_D-\varepsilon_A$. As mentioned in the previous section, the incremental elastic strain $\Delta\varepsilon_1^e$ has nearly no change in the same cyclic loading simulation, and thus hysteresis loops have a unified resilient modulus. A relatively large plastic strain is accumulated in the first loading but $\Delta\varepsilon_1^p$ reduces to zero as the cyclic loading continues. Fig. 7b presents

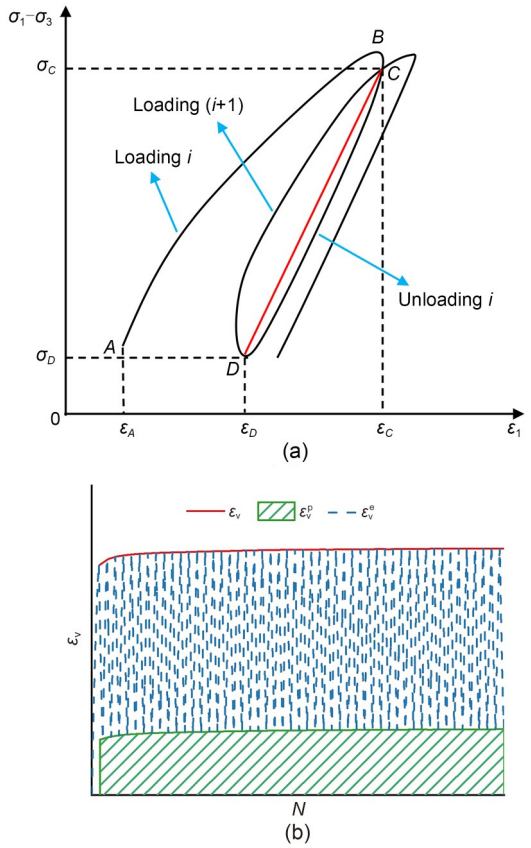

Fig. 7 Strain evolution during cyclic loading: (a) hysteresis loop; (b) volumetric strain evolving with N

the evolution of elastic and plastic volumetric strains. The elastic volumetric strain fluctuates with practically the same amplitude during the cyclic loading, while the accumulated plastic strain grows slowly and tends to eventual stability. The growth rate of the accumulative plastic strain gradually decreases as the number of cycles N increases, and both axial plastic strain and volumetric plastic strain satisfy the equation (Zhang D et al., 2019):

$$\varepsilon^{\mathrm{p}}=\frac{\alpha N^{\beta}}{1+\gamma N^{\beta}}, \tag{8}$$

where α, β, and γ are fitting parameters.

The macro mechanics of granular materials are closely connected with particle scale behaviors, such as particle rearrangement and breakage (Zhang LK et al., 2019; Lin et al., 2022). In this section, we investigate, from a microscopic perspective, the hysteretic behavior of crushable particle material under cyclic loading. For concision, the specimen under P=1.5 MPa, S_{L}=0.7, and U_{a}=1.0 is taken as an example here, and the similar evolution of other specimens is omitted from this study. The evolution of axial strain and volumetric strain of the sample is depicted in Fig. 8. Both fitting curves of axial strain $\varepsilon_{1}^{\mathrm{p}}$ and volumetric strain $\varepsilon_{\mathrm{v}}^{\mathrm{p}}$ agree well with the simulation results, where the fitting parameters in Eq. (8) for $\varepsilon_{1}^{\mathrm{p}}$ are α=0.03583, β=0.42066, γ=1.41605, and R^2=0.9997, respectively; correspondingly, parameters for $\varepsilon_{\mathrm{v}}^{\mathrm{p}}$ are α=0.01997, β=0.31868, γ=3.47764, and R^2=0.9986, respectively.

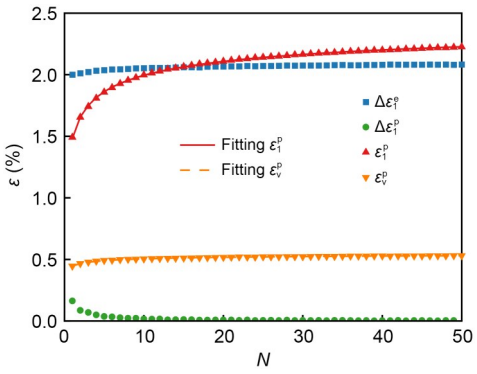

Fig. 8 Relations between the axial strain and the number of cycles N and between the volumetric strain and N (P=1.5 MPa, S_{L}=0.7, U_{a}=1.0)

3.1 Coordination number and porosity

To further understand the underlying mechanism of hysteretic behavior, we analyze the coordination number and porosity of the specimen. The coordination number CN is an effective measure for representing the specimen density and stability, as well as features of its internal structure. The coordination number of a granular assembly is the average number of contacts. However, particles with contacts less than 2 can make no contribution to the stability of the stress state (Thornton, 2000). Thus, the effective coordination number $\mathrm{CN}_{\mathrm{eff}}$ for a granular assembly can be written as:

$$\mathrm{CN}_{\mathrm{eff}}=\frac{2C-N_1}{N_{\mathrm{p}}-N_1-N_0}, \tag{9}$$

where C is the total number of contacts; N_{p} is the total number of particles; N_0 and N_1 are the numbers of particles with coordination numbers of 0 and 1, respectively. Particles with contacts less than 2 are usually small particles and, for brevity, are termed the rattlers in this study. The porosity n_0 of the specimen can be computed by dividing the total volume of particles V_{s} by the total volume of the specimen V, i.e., $n_0=V_{\mathrm{s}}/V$. Analogous to $\mathrm{CN}_{\mathrm{eff}}$, and ignoring the particles without force-carrying capability, the effective porosity n_{eff} is defined as:

$$n_{\mathrm{eff}}=\left(1-\frac{V_{\mathrm{s}}-V_{\mathrm{f}}}{V}\right)\times 100\%, \tag{10}$$

where V_{f} is the volume including particles with contacts less than 2.

As shown in Fig. 9, we compute the effective coordination number and effective porosity at the end of each load and plot them by solid lines. Values at the end of each unloading are represented by dotted lines. As the number of cycles increases, the effective coordination number $\mathrm{CN}_{\mathrm{eff}}$ at the end of loading first increases and then stabilizes; however, that of unloading keeps decreasing and the change rate is reduced. It suggests that some of the rattlers participate in contact force transmission, and that enhances the stability of the structure. The effective coordination number decreases due to some particles with few contacts turning into rattlers during unloading. The difference between loading and unloading curves exists during the whole cyclic loading process, and manifests itself in the change in the number of rattlers. The effective coordination number increases fast in the first few cycles

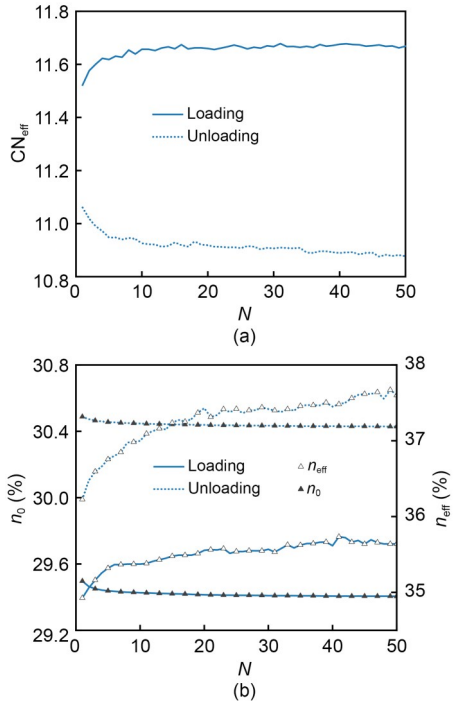

Fig. 9 Coordination number (a) and porosity evolution (b) of the specimen under different numbers of cycles N (P= 1.5 MPa, S_L=0.7, U_a=1.0)

and then its change rate slows down. This change coincides with the evolution of plastic strain ε_1^p, which implies the movement of hysteresis loops as the cyclic loading continues. Moreover, the number of effective particles changing into rattlers is more than that of rattlers turning into effective particles, which probably produces the residual strain.

During cyclic loading, the porosity n of the specimen keeps decreasing. The voids in the specimen are relatively large at first, and particles can adjust their positions and contact each other, and thus the porosity decreases rapidly. After a few cycles, the voids become small and there is limited space for particle rearrangement. As cyclic loading continues, large particles are prone to break into small fragments which can further fill in the gaps; therefore, the volume keeps contracting at a low rate. However, no matter when loading or unloading, the effective porosity n_{eff} of the specimen increases and then keeps constant after a large number of cycles, which is similar to the evolution of volumetric strain ε_v^p. The increasing effective porosity suggests a growing number of rattlers. The curve of unloading being higher than that of loading indicates that many more particles lose contacts when unloading and make no contribution to the stability of the structure. The difference between loading and unloading curves remains almost constant, indicating that the change in the porosity of each cycle is the same and making the hysteresis loops of volumetric strain parallel to each other. The rate of change reduces after a certain number of cycles and thus the hysteresis loops coincide.

3.2 Particle breakage

Generally, particle breakage is accompanied by particle rearrangement during the whole shearing (Ueng and Chen, 2000; Coop et al., 2004; Li et al., 2016; Ma et al., 2018). The particle breakage distributions after triaxial compression tests and cyclic loading tests under four confining pressures are presented in Fig. 10. It is observed that the amount of particle breakage increases with the confining pressure. The particle breakage is more significant when the specimen is subjected to cyclic loading under a higher stress level and larger confining pressure.

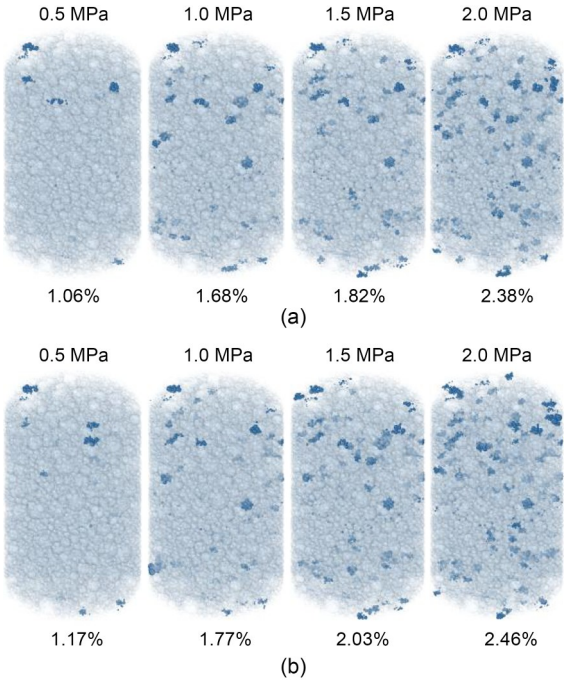

Fig. 10 Particle breakage distributions of specimens under different confining pressures: (a) conventional triaxial compression tests; (b) cyclic loading tests (S_L=0.7, U_a=1.0)

The particle breakage ratio defined by Marsal (1967) is adopted to measure the degree of particle breakage:

$$B_{\mathrm{m}}=\sum\left|B_{\mathrm{ma},i}-B_{\mathrm{mb},i}\right|, \tag{11}$$

where $B_{\mathrm{ma},i}$ and $B_{\mathrm{mb},i}$ correspond to the differences of percentage retained on the initial and final grain-size distributions for each sieve size, respectively. At the end of the triaxial compression loading, the particle breakage ratios B_{m} for four different confining pressures are 1.06%, 1.68%, 1.82%, and 2.38%, respectively. While B_{m} at the end of four cyclic loading tests (S_{L}=0.7, U_{a}=1.0) are 1.17%, 1.77%, 2.03%, and 2.46%, respectively. It is concluded that a rising confining pressure will lead to an increase in B_{m}, and cyclic loading can intensify the degree of particle breakage.

Recalling Fig. 9, the coordination number and the porosity have little change with the number of cycles after 10 cyclic loadings. It can be inferred that there is no significant particle breakage occurring during the later cyclic loading process and small particles in voids change positions more easily. Sectional views of the specimen at the 10th and 50th cyclic loadings are shown in Fig. 11. As shown in the dotted boxes of Fig. 11a, the number and position of small particles in voids are different from those in Fig. 11b, suggesting that small particles are rearranged during the cyclic loading test. Voids in the specimen may expand or be squeezed due to changed external loadings, and thus small particles in voids are prone to move. After a certain number of cycles (about 10 times in this case), the space for particle motion becomes less. Therefore, the deformation of granular assembly tends to stabilize after a few cyclic loadings, resulting in the overlap of hysteresis loops.

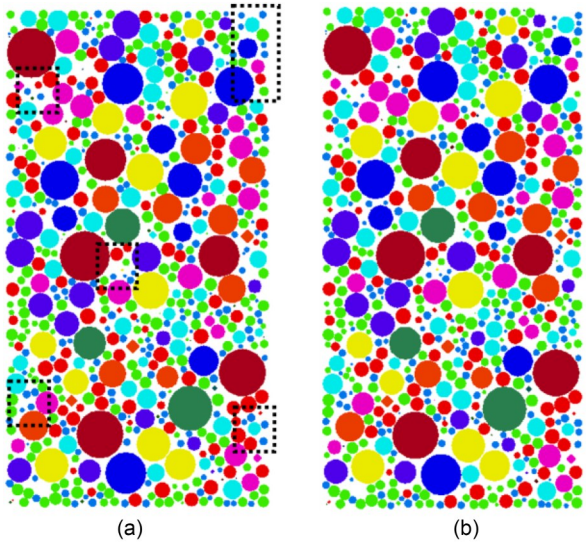

Fig. 11 Particle arrangements in the specimen (P=1.5 MPa, S_{L}=0.7, U_{a}=1.0) at different numbers of cycles: (a) N=10; (b) N=50

Considering the coordination number, the porosity, and the particle breakage ratio, the effect of microstructure evolution on macro responses becomes clear. In the early stage of loading, the specimen has enough voids for particles to rearrange, and some rattlers will fill the voids and undertake force transmissions. In this phase, the specimen shows volume contraction due to the increased interparticle restraints, and the strength of shearing resistance has been enhanced. As loading continues, some particles may be crushed, and fragments will further fill in voids so that the porosity keeps decreasing. The density of the specimen fluctuates with cyclic loading. However, the effective porosity shows a rising tendency. Many particles may rearrange and lose contacts during cyclic loading, inducing a decrease in effective coordination number and may result in unrecoverable strain at the macroscopic level. The evolution of the effective coordination number and the porosity is generally stabilized after many cycles and thus hysteresis loops gradually overlap. In the meantime, the degree of particle breakage is relatively low and thus the granular media can sustain the shear strength after a large number of cycles.

4 Deformation characteristics under different loading conditions

4.1 Effect of loading conditions on hysteresis loops

To further explore the deformation characteristics of cyclic loading, the stress and strain responses of other specimens under different cyclic loading conditions are shown in Fig. 12. Broadly, hysteresis loops in Fig. 12a are parallel to each other in corresponding tests and gradually approach (even coincide) in the later cycles. The inclinations of hysteresis loops increase with the increasing confining pressures. While the unloading–reloading curves of volumetric strain nearly have the same tilting degree (the right subplot of Fig. 12a). As shown in Fig. 12b, the offsets of hysteresis loops under the same number of cycles are positively correlated with stress levels. When the specimen is under a low-stress level, the hysteresis loops are nearly unchanged and can be regarded as approximating elasticity. The volumetric strains exhibit similar

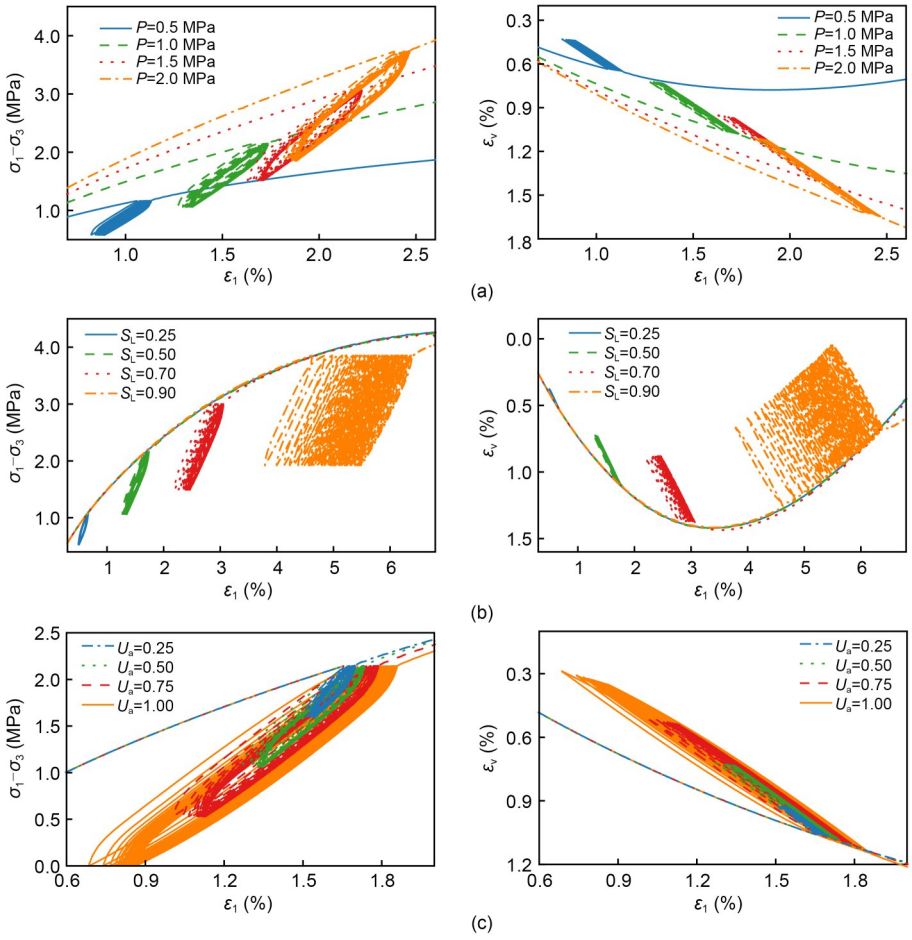

Fig. 12 Effect of cyclic loading conditions on hysteresis loops evolution: (a) confining pressures (S_L=0.5, U_a=0.5); (b) stress levels (P=1.0 MPa, U_a=0.5); (c) amplitudes of the unloading–reloading processes (P=1.0 MPa, S_L=0.5)

rules but more significant dilatation at higher stress levels. In Fig. 12c, the inclination of hysteresis loops is slightly reduced as the amplitude of cyclic loading increases. Analogously, the offsets of hysteresis loops under the same number of cycles have a positive correlation with the amplitude of cyclic loading, but the degree of offsets is smaller than that caused by stress levels.

The evolution of plastic axial strains under different confining pressures, stress levels, and the amplitudes of cyclic loadings are shown in Fig. 13. As the confining pressure increases, the plastic strains accumulate with the increase in the number of cycles. The same law is observed when the stress level increases but the specimens with high amplitudes of cyclic loadings remain with few plastic strains at the end of unloading. As mentioned in Section 3, the plastic strain follows Eq. (8). It is noticed that the case of S_L=0.25 is not considered in the fitting due to there being no plastic strain accumulation under the low-stress level. The effect of these loading conditions on the plastic volumetric strain ε_v^p is similar, and, for brevity, details will not be covered here.

4.2 Resilient modulus

The initial Young's modulus E_i can be expressed as a function of the confining pressure P as proposed by Janbu (1963):

$$E_i = KP_a\left(\frac{P}{P_a}\right)^n, \tag{12}$$

where P_a is the atmospheric pressure (P_a=101.4 kPa), K is the modulus number, and n is the variation rate of E_i with confining pressure. Similarly, the resilient modulus E_{ur} also meets the relationship as follows (Duncan and Chang, 1970):

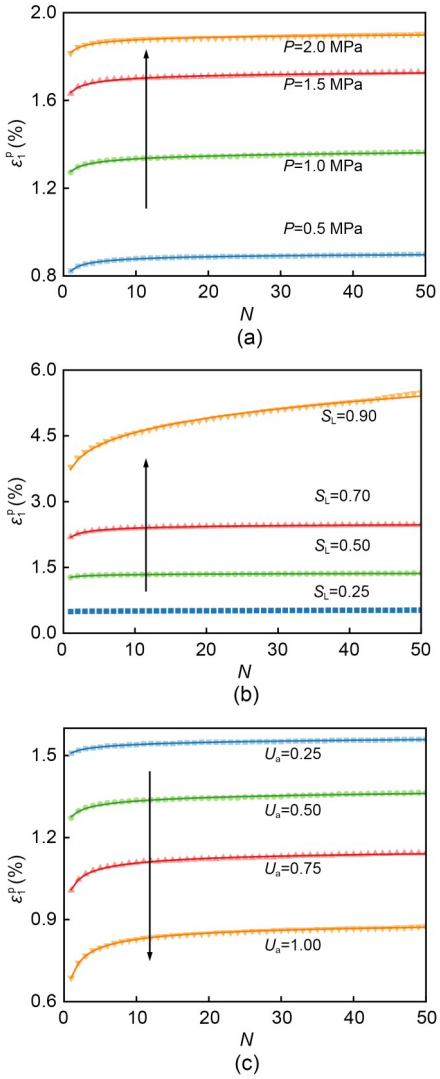

Fig. 13 Evolution of axial cumulative plastic strains under different loading conditions: (a) confining pressures; (b) stress levels; (c) amplitudes of cyclic loadings

$$E_{ur}=K_{ur}P_a\left(\frac{P}{P_a}\right)^{n_{ur}}, \tag{13}$$

where K_{ur} is the unloading–reloading modulus number; n_{ur} is a dimensionless index.

The relations of E_i–P and E_{ur}–P are plotted in Figs. 14 and 15, respectively, where lg$K$ and lgK_{ur} are the intercepts, and n and n_{ur} are the slopes of the lines. It is noticed that at the stress level of 0.7 and the amplitude of the unloading–reloading of 0.5, K and n for E_i are different to K_{ur} and n_{ur} for E_{ur}.

In addition, the stress levels S_L and the amplitudes of the unloading–reloading U_a have similar effects on the evolution of the resilient moduli (Figs. 16 and 17). Under the same confining pressure condition, E_{ur} decreases with increasing S_L and U_a. Therefore, the effects of S_L and U_a can be taken as power functions of the resilient modulus, like $E_{ur}=\alpha_1 S_L^{\alpha_2}$ and $E_{ur}=\alpha_1 U_a^{\alpha_2}$, and can be considered in the expression of E_{ur}. Here we assume the function E_{ur} as:

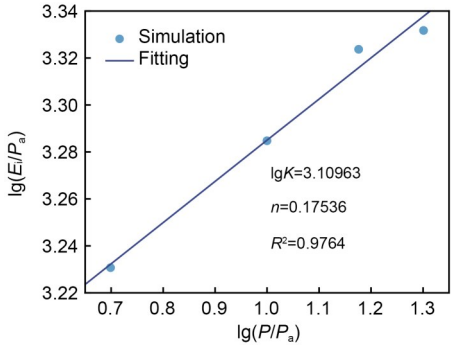

Fig. 14 Initial Young's moduli under different confining pressures (S_L=0.7, U_a=0.5)

$$E_{ur}=\alpha_1 P_a\left(\frac{P}{P_a}\right)^{\alpha_2} S_L^{\alpha_3} U_a^{\alpha_4}, \tag{14}$$

where α_1=968.08, α_2=0.22344, α_3=−0.38318, and α_4=−0.40809 are fitting parameters. This equation is also in good agreement with the rest groups of cyclic loading tests (R^2=0.9644), verifying the hypothesis. It is noticed that the resilient modulus is insensitive to the number of cycles, which is consistent with other studies (Indraratna et al., 2010; Fu et al., 2017; Xia et al., 2021).

5 Conclusions

A series of DEM simulations of breakable particles is conducted to investigate the deformation characteristics of rockfill material under cyclic loading. The effect on hysteretic behavior of loading conditions, such as confining pressure, stress level, the amplitude of cyclic loading, and the number of cycles, is analyzed. The evolution functions of plastic strain and resilient modulus are proposed based on the results of numerical analysis. The main conclusions of this study are summarized as follows:

1. Hysteresis loops exist after each loading–unloading process, and they are parallel to each other and gradually coincide due to particle rearrangement.

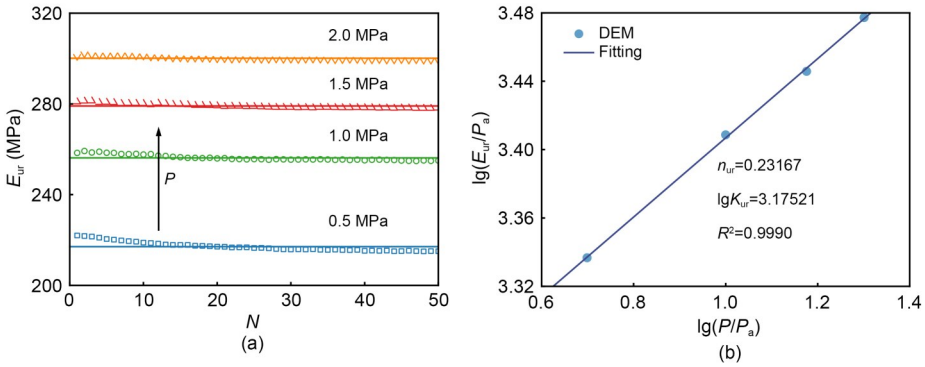

Fig. 15 Evolution of resilient modulus under different confining pressures (S_L=0.7, U_a=0.5): (a) E_{ur} evolving with N; (b) E_{ur} evolving with P

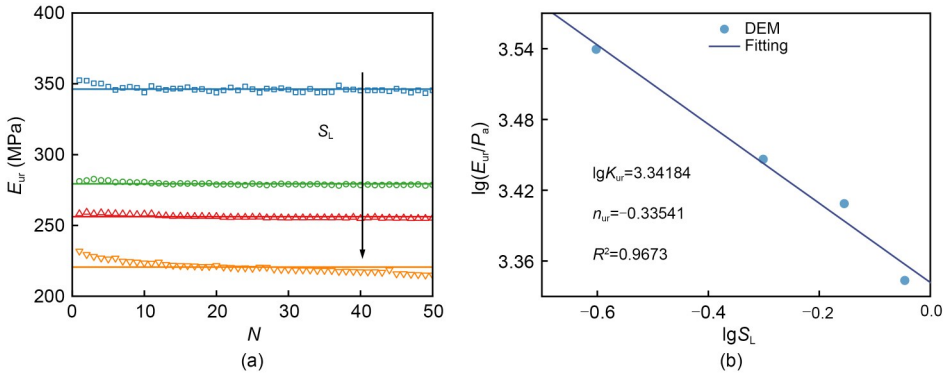

Fig. 16 Evolution of resilient modulus under different stress levels (P=1.0 MPa, U_a=0.5): (a) E_{ur} evolving with N; (b) E_{ur} evolving with S_L

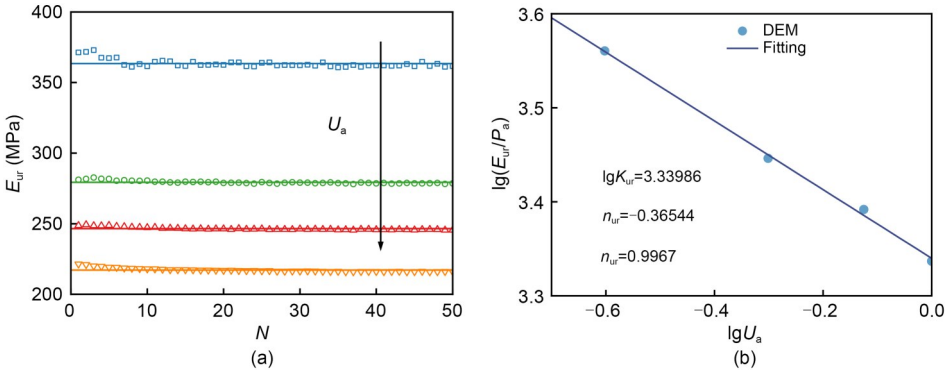

Fig. 17 Evolution of resilient modulus under different amplitudes of cyclic loadings (P=1.0 MPa, S_L=0.5): (a) E_{ur} evolving with N; (b) E_{ur} evolving with U_a

The slop of hysteresis loops increases with confining pressure but decreases with stress level. In addition, more plastic strains accumulate with cyclic loading at a higher stress level, displaying looser spacing between hysteresis loops. Although volumetric strains have similar laws with stress evolution, the hysteretic behavior they show is limited.

2. The hysteretic behavior of cyclic loading is analyzed from a microscale view. The rattlers accumulated during each cyclic loading can cause the generation of a residual strain. The difference in porosity between loading and unloading remains constant, and thus the offsets of hysteresis loops for volumetric strain are small. The slowing down change in porosity

during cyclic loading results in coincidence after a large number of cycles. The particle breakage also plays a part in the hysteretic behavior, which invokes an increase in small particles and the local structure rearrangement.

3. The deformation of a rockfill specimen can be separated into a periodical elastic strain and an accumulated plastic strain, where the plastic deformation grows monotonically and gradually stabilizes. The relationship between the number of cycles and the plastic strain accumulation is closely connected with confining pressure P, stress level S_L, and the amplitude of cyclic loading U_a. A function considering the effect of P, S_L, and U_a is proposed to describe the resilient modulus. The proposed function is expected to be applied in practical engineering cases, such as a pumped storage power station project, by being imbedded into the finite numerical analysis program. The feasibility and application prospects need further careful verification in the future.

Acknowledgments

This work is supported by the National Natural Science Foundation of China (Nos. 52179141, 51825905, and U1865204) and the Foundation of Power China Chengdu Engineering Co., Ltd. (No. CD2C20220155). The numerical calculations in this study have been done on the supercomputing system in the Supercomputing Center of Wuhan University, China.

Author contributions

Wei ZHOU received funding and designed the research. Gang MA designed the experimental and numerical tests. Mingchun LIN and Jian ZHOU processed the corresponding data. Mingchun LIN wrote the first draft of the manuscript. Gang MA, Guanqi WANG, and Ni AN helped to organize the manuscript. Mingchun LIN revised and edited the final version.

Conflict of interest

Mingchun LIN, Guanqi WANG, Jian ZHOU, Wei ZHOU, Ni AN, and Gang MA declare that they have no conflict of interest.

References

Ai J, Chen JF, Rotter JM, et al., 2011. Assessment of rolling resistance models in discrete element simulations. *Powder Technology*, 206(3):269-282. https://doi.org/10.1016/j.powtec.2010.09.030

Athanassiadis AG, Miskin MZ, Kaplan P, et al., 2014. Particle shape effects on the stress response of granular packings. *Soft Matter*, 10(1):48-59. https://doi.org/10.1039/C3SM52047A

Bagi K, 1996. Stress and strain in granular assemblies. *Mechanics of Materials*, 22(3):165-177. https://doi.org/10.1016/0167-6636(95)00044-5

Belheine N, Plassiard JP, Donzé FV, et al., 2009. Numerical simulation of drained triaxial test using 3D discrete element modeling. *Computers and Geotechnics*, 36(1-2):320-331. https://doi.org/10.1016/j.compgeo.2008.02.003

Ben-Nun O, Einav I, 2010. The role of self-organization during confined comminution of granular materials. *Philosophical Transactions of the Royal Society A: Mathematical, Physical and Engineering Sciences*, 368(1910):231-247. https://doi.org/10.1098/rsta.2009.0205

Borkovec M, de Paris W, Peikert R, 1994. The fractal dimension of the Apollonian sphere packing. *Fractals*, 2(4):521-526. https://doi.org/10.1142/S0218348X94000739

Cai YQ, Sun Q, Guo L, et al., 2015. Permanent deformation characteristics of saturated sand under cyclic loading. *Canadian Geotechnical Journal*, 52(6):795-807. https://doi.org/10.1139/cgj-2014-0341

Chen SS, Fu ZZ, Wei KM, et al., 2016. Seismic responses of high concrete face rockfill dams: a case study. *Water Science and Engineering*, 9(3):195-204. https://doi.org/10.1016/j.wse.2016.09.002

Chen Y, Ma G, Zhou W, et al., 2021. An enhanced tool for probing the microscopic behavior of granular materials based on X-ray micro-CT and FDEM. *Computers and Geotechnics*, 132:103974. https://doi.org/10.1016/j.compgeo.2020.103974

Ciantia MO, Arroyo M, Calvetti F, et al., 2015. An approach to enhance efficiency of DEM modelling of soils with crushable grains. *Géotechnique*, 65(2):91-110. https://doi.org/10.1680/geot.13.P.218

Coop MR, Sorensen KK, Freitas TB, et al., 2004. Particle breakage during shearing of a carbonate sand. *Géotechnique*, 54(3):157-163. https://doi.org/10.1680/geot.2004.54.3.157

Dahal B, Mishra D, 2020. Discrete element modeling of permanent deformation accumulation in railroad ballast considering particle breakage. *Frontiers in Built Environment*, 5:145. https://doi.org/10.3389/fbuil.2019.00145

de Bono J, McDowell G, 2016. Particle breakage criteria in discrete-element modelling. *Géotechnique*, 66(12):1014-1027. https://doi.org/10.1680/jgeot.15.P.280

Duncan JM, Chang CY, 1970. Nonlinear analysis of stress and strain in soils. *Journal of the Soil Mechanics and Foundations Division*, 96(5):1629-1653. https://doi.org/10.1061/JSFEAQ.0001458

Einav I, 2007. Breakage mechanics—part I: theory. *Journal of the Mechanics and Physics of Solids*, 55(6):1274-1297. https://doi.org/10.1016/j.jmps.2006.11.003

Estrada N, Azéma E, Radjai F, et al., 2011. Identification of rolling resistance as a shape parameter in sheared granular media. *Physical Review E*, 84(1):011306. https://doi.org/10.1103/PhysRevE.84.011306

Fu ZZ, Chen SS, Han HQ, 2017. Experimental investigations on the residual strain behavior of a rockfill material

subjected to dynamic loading. *Journal of Materials in Civil Engineering*, 29(5):04016278. https://doi.org/10.1061/%28ASCE%29MT.1943-5533.0001816

Gu C, Zhan Y, Wang J, et al., 2020. Resilient and permanent deformation of unsaturated unbound granular materials under cyclic loading by the large-scale triaxial tests. *Acta Geotechnica*, 15(12):3343-3356. https://doi.org/10.1007/s11440-020-00966-0

Harireche O, McDowell GR, 2003. Discrete element modelling of cyclic loading of crushable aggreates. *Granular Matter*, 5(3):147-151. https://doi.org/10.1007/s10035-003-0143-9

Huang QS, Zhou W, Ma G, et al., 2020. Experimental and numerical investigation of Weibullian behavior of grain crushing strength. *Geoscience Frontiers*, 11(2):401-411. https://doi.org/10.1016/j.gsf.2019.07.007

Indraratna B, Thakur PK, Vinod JS, 2010. Experimental and numerical study of railway ballast behavior under cyclic loading. *International Journal of Geomechanics*, 10(4):136-144. https://doi.org/10.1061/%28ASCE%29GM.1943-5622.0000055

Itasca Consulting Group Inc., 2014. Particle Flow Code in 3 Dimensions (PFC3D), Version 5.0. Itasca Consulting Inc., Minneapolis, USA, p.2199-2216.

Iwashita K, Oda M, 1998. Rolling resistance at contacts in simulation of shear band development by DEM. *Journal of Engineering Mechanics*, 124(3):285-292. https://doi.org/10.1061/(ASCE)0733-9399(1998)124:3(285)

Iwashita K, Oda M, 2000. Micro-deformation mechanism of shear banding process based on modified distinct element method. *Powder Technology*, 109(1-3):192-205. https://doi.org/10.1016/S0032-5910(99)00236-3

Janbu N, 1963. Soil compressibility as determined by oedometer and triaxial tests. Proceedings of the European Conference on Soil Mechanics and Foundation Engineering, p.19-25.

Jiang MJ, Zhang A, Li T, 2019. Distinct element analysis of the microstructure evolution in granular soils under cyclic loading. *Granular Matter*, 21(2):39. https://doi.org/10.1007/s10035-019-0892-8

Jin Z, Lu Z, Yang Y, 2021. Numerical analysis of column collapse by smoothed particle hydrodynamics with an advanced critical state-based model. *Journal of Zhejiang University-SCIENCE A (Applied Physics & Engineering)*, 22(11):882-893. https://doi.org/10.1631/jzus.A2000598

Lee DM, 1992. The Angles of Friction of Granular Fills. PhD Thesis, University of Cambridge, Cambridge, UK.

Li XM, Li HW, Zheng MS, et al., 2016. Research on particle breakage of rockfill material based on modified Duncan-Chang model. *Chinese Journal of Rock Mechanics and Engineering*, 35(S1):2695-2701 (in Chinese). https://doi.org/10.13722/j.cnki.jrme.2014.1716

Lin MC, Zhou W, Liu JY, et al., 2022. A topological view on microscopic structural evolution for granular material under loading and unloading path. *Computers and Geotechnics*, 141:104530. https://doi.org/10.1016/j.compgeo.2021.104530

Liu H, Xiao JL, Wang P, et al., 2018. Experimental investigation of the characteristics of a granular ballast bed under cyclic longitudinal loading. *Construction and Building Materials*, 163:214-224. https://doi.org/10.1016/j.conbuildmat.2017.12.037

Liu HB, Zou DG, Liu JM, 2014. Constitutive modeling of dense gravelly soils subjected to cyclic loading. *International Journal for Numerical and Analytical Methods in Geomechanics*, 38(14):1503-1518. https://doi.org/10.1002/nag.2269

Liu YM, Liu HB, Mao HJ, 2018. The influence of rolling resistance on the stress-dilatancy and fabric anisotropy of granular materials. *Granular Matter*, 20(1):12. https://doi.org/10.1007/s10035-017-0780-z

Lobo-Guerrero S, Vallejo LE, 2006. Discrete element method analysis of railtrack ballast degradation during cyclic loading. *Granular Matter*, 8(3):195-204. https://doi.org/10.1007/s10035-006-0006-2

Lu M, McDowell GR, 2007. The importance of modelling ballast particle shape in the discrete element method. *Granular Matter*, 9(1):69-80. https://doi.org/10.1007/s10035-006-0021-3

Ma G, Regueiro RA, Zhou W, et al., 2018. Role of particle crushing on particle kinematics and shear banding in granular materials. *Acta Geotechnica*, 13(3):601-618. https://doi.org/10.1007/s11440-017-0621-6

Ma G, Chen Y, Yao FH, et al., 2019. Evolution of particle size and shape towards a steady state: insights from FDEM simulations of crushable granular materials. *Computers and Geotechnics*, 112:147-158. https://doi.org/10.1016/j.compgeo.2019.04.022

Marsal RJ, 1967. Large scale testing of rockfill materials. *Journal of the Soil Mechanics and Foundations Division*, 93(2):27-43. https://doi.org/10.1061/JSFEAQ.0000958

McDowell GR, Bolton MD, 1998. On the micromechanics of crushable aggregates. *Géotechnique*, 48(5):667-679. https://doi.org/10.1680/geot.1998.48.5.667

MWR (Ministry of Water Resources of the People's Republic of China), 1999. Specification of Soil Test, SL 237-1999. National Standards of the People's Republic of China (in Chinese).

O'Sullivan C, Cui L, O'Neill SC, 2008. Discrete element analysis of the response of granular materials during cyclic loading. *Soils and Foundations*, 48(4):511-530. https://doi.org/10.3208/sandf.48.511

Potyondy DO, Cundall PA, 2004. A bonded-particle model for rock. *International Journal of Rock Mechanics and Mining Sciences*, 41(8):1329-1364. https://doi.org/10.1016/j.ijrmms.2004.09.011

Santos AP, Bolintineanu DS, Grest GS, et al., 2020. Granular packings with sliding, rolling, and twisting friction. *Physical Review E*, 102(3):032903. https://doi.org/10.1103/PhysRevE.102.032903

Sazzad M, 2014. Micro-scale behavior of granular materials during cyclic loading. *Particuology*, 16:132-141. https://doi.org/10.1016/j.partic.2013.12.005

Sazzad M, Suzuki K, 2010. Micromechanical behavior of granular materials with inherent anisotropy under cyclic loading using 2D DEM. *Granular Matter*, 12(6):597-605. https://doi.org/10.1007/s10035-010-0200-0

Sazzad M, Suzuki K, 2011. Effect of interparticle friction on

the cyclic behavior of granular materials using 2D DEM. *Journal of Geotechnical and Geoenvironmental Engineering*, 137(5):545-549. https://doi.org/10.1061/%28ASCE%29GT.1943-5606.0000441

Scaioni M, Marsella M, Crosetto M, et al., 2018. Geodetic and remote-sensing sensors for dam deformation monitoring. *Sensors*, 18(11):3682. https://doi.org/10.3390/s18113682

Skrzypkowski K, 2020. Decreasing mining losses for the room and pillar method by replacing the inter-room pillars by the construction of wooden cribs filled with waste rocks. *Energies*, 13(14):3564. https://doi.org/10.3390/en13143564

Skrzypkowski K, 2021. Determination of the backfilling time for the zinc and lead ore deposits with application of the BackfillCAD model. *Energies*, 14(11):3186. https://doi.org/10.3390/en14113186

Sun QD, Indraratna B, Nimbalkar S, 2014. Effect of cyclic loading frequency on the permanent deformation and degradation of railway ballast. *Géotechnique*, 64(9):746-751. https://doi.org/10.1680/geot.14.T.015

Tapias M, Alonso EE, Gili J, 2015. A particle model for rockfill behaviour. *Géotechnique*, 65(12):975-994. https://doi.org/10.1680/jgeot.14.P.170

Thornton C, 2000. Numerical simulations of deviatoric shear deformation of granular media. *Géotechnique*, 50(1):43-53. https://doi.org/10.1680/geot.2000.50.1.43

Ueng TS, Chen TJ, 2000. Energy aspects of particle breakage in drained shear of sands. *Géotechnique*, 50(1):65-72. https://doi.org/10.1680/geot.2000.50.1.65

Wei JT, Huang DR, Wang G, 2020. Fabric evolution of granular soils under multidirectional cyclic loading. *Acta Geotechnica*, 15(9):2529-2543. https://doi.org/10.1007/s11440-020-00942-8

Wensrich CM, Katterfeld A, 2012. Rolling friction as a technique for modelling particle shape in DEM. *Powder Technology*, 217:409-417. https://doi.org/10.1016/j.powtec.2011.10.057

Xia PX, Shao LT, Deng W, 2021. Mechanism study of the evolution of quasi-elasticity of granular soil during cyclic loading. *Granular Matter*, 23(4):84. https://doi.org/10.1007/s10035-021-01157-8

Xiao Y, Liu H, Zhang WG, et al., 2016. Testing and modeling of rockfill materials: a review. *Journal of Rock Mechanics and Geotechnical Engineering*, 8(3):415-422. https://doi.org/10.1016/j.jrmge.2015.09.009

Xiao Y, Meng MQ, Daouadji A, et al., 2020. Effects of particle size on crushing and deformation behaviors of rockfill materials. *Geoscience Frontiers*, 11(2):375-388. https://doi.org/10.1016/j.gsf.2018.10.010

Xu K, Zhou W, Ma G, 2020. Influence of particle breakage on scale effect of filling characteristics of rockfill material. *Chinese Journal of Geotechnical Engineering*, 42(6):1013-1022 (in Chinese). https://doi.org/10.11779/CJGE202006004

Yin ZY, Jin YF, Zhang X, 2021. Large deformation analysis in geohazards and geotechnics. *Journal of Zhejiang University-SCIENCE A (Applied Physics & Engineering)*, 22(11):851-855. https://doi.org/10.1631/jzus.A21LDGG1

Yuan WH, Wang HC, Liu K, et al., 2021. Analysis of large deformation geotechnical problems using implicit generalized interpolation material point method. *Journal of Zhejiang University-SCIENCE A (Applied Physics & Engineering)*, 22(11):909-923. https://doi.org/10.1631/jzus.A2100219

Zhang D, Li QM, Liu EL, et al., 2019. Dynamic properties of frozen silty soils with different coarse-grained contents subjected to cyclic triaxial loading. *Cold Regions Science and Technology*, 157:64-85. https://doi.org/10.1016/j.coldregions.2018.09.010

Zhang H, Jing YL, Chen JK, et al., 2022. Characteristics and causes of crest cracking on a high core-wall rockfill dam: a case study. *Engineering Geology*, 297:106488. https://doi.org/10.1016/j.enggeo.2021.106488

Zhang LK, Wang R, Zhang JM, et al., 2019. Experimental study on dynamic deformation characteristics of rockfill materials under different stress paths. *Engineering Mechanics*, 36(3):114-120. https://doi.org/10.6052/j.issn.1000-4750.2018.01.0072

Zhao SW, Evans TM, Zhou XW, 2018. Shear-induced anisotropy of granular materials with rolling resistance and particle shape effects. *International Journal of Solids and Structures*, 150:268-281. https://doi.org/10.1016/j.ijsolstr.2018.06.024

Zhou B, Ku Q, Li CH, et al., 2022. Single-particle crushing behaviour of carbonate sands studied by X-ray microtomography and a combined finite–discrete element method. *Acta Geotechnica*, 17(8):3195-3209. https://doi.org/10.1007/s11440-022-01469-w

Zhou W, Li SL, Ma G, et al., 2016a. Assessment of the crest cracks of the Pubugou rockfill dam based on parameters back analysis. *Geomechanics and Engineering*, 11(4):571-585. https://doi.org/10.12989/gae.2016.11.4.571

Zhou W, Li SL, Ma G, et al., 2016b. Parameters inversion of high central core rockfill dams based on a novel genetic algorithm. *Science China Technological Sciences*, 59(5):783-794. https://doi.org/10.1007/s11431-016-6017-2

Zhou W, Yang LF, Ma G, et al., 2017. DEM modeling of shear bands in crushable and irregularly shaped granular materials. *Granular Matter*, 19(2):25. https://doi.org/10.1007/s10035-017-0712-y

Zhou W, Xu K, Ma G, et al., 2019. On the breakage function for constructing the fragment replacement modes. *Particuology*, 44:207-217. https://doi.org/10.1016/j.partic.2018.08.006

Zhou W, Wang D, Ma G, et al., 2020. Discrete element modeling of particle breakage considering different fragment replacement modes. *Powder Technology*, 360:312-323. https://doi.org/10.1016/j.powtec.2019.10.002

Zou YX, Ma G, Mei JZ, et al., 2022. Microscopic origin of shape-dependent shear strength of granular materials: a granular dynamics perspective. *Acta Geotechnica*, 17(7):2697-2710. https://doi.org/10.1007/s11440-021-01403-6